Award Information

Award Numbers	N00014-11-1-0605 and N00014-16-1-2405
Title of Research	Hot Corrosion and High Temperature Oxidation of Al_2O_3 Scale-Forming Alloys
Principal Investigator	A. H. Heuer
Organization	Case Western Reserve University

Technical Section

Introduction

This report summarizes research on two related ONR projects. Award number N00014-11-1-0605, supported roughly the first third of our ONR effort, and was mainly devoted to the effect of 5 at% additions of Cr and/or Pt on the Type II hot corrosion behavior of β Ni-36Al, an alumina scale-forming alloy, at 700 ^{o}C. Award number N00014-16-1-2405, a continuation of N00014-11-1-0605, was primarily devoted to the high temperature (1100 ^{o}C– 1400 ^{o}C) oxidation of γ/γ' Ni-20Al-5 Cr bond coat alloys; this latter effort had been started on the -0605 program. The -2405 program focused primarily on the effect of small (0.05 at %) additions of the so-called Reactive Elements, Y and Hf to the base γ/γ' Ni20Al-5Cr alloy. The high temperature oxidation of the γ/γ' alloys will be discussed first.

I.1 High temperature oxidation of γ/γ' NiAlCr bond coat alloys

Al_2O_3 scales formed for 72 hrs in air at 1100 ^{o}C on γ/γ' NiAlCr bond coat alloys containing small additions of the Reactive Elements (REs), Hf and Y, as well as Si (not a RE), were studied. The thickest scale was found in the Ni-20Al-5Cr base alloy, as expected, while much thinner scales formed due to the RE additions to the Ni-20Al-5Cr-0.05Hf-0.05Y and

REPORT DOCUMENTATION PAGE

Form Approved
OMB No. 0704-0188

1. REPORT DATE (DD-MM-YYYY)	2. REPORT TYPE	3. DATES COVERED (From - To)
25/05/2018	Final	5/1/2011-3/31/2018

4. TITLE AND SUBTITLE
Hot Corrosion Studies of Advanced Alloys

5a. CONTRACT NUMBER
N/A

5b. GRANT NUMBER
N00014-16-1-2405; N00014-11-1-0605

5c. PROGRAM ELEMENT NUMBER

6. AUTHOR(S)
Heuer, Arthur, H

5d. PROJECT NUMBER

5e. TASK NUMBER

5f. WORK UNIT NUMBER

7. PERFORMING ORGANIZATION NAME(S) AND ADDRESS(ES)
Case Western Reserve University
10900 Euclid Ave., Cleveland, OH 44106-1712

8. PERFORMING ORGANIZATION REPORT NUMBER

9. SPONSORING/MONITORING AGENCY NAME(S) AND ADDRESS(ES)
Office of Naval Research
ONR Reg. Office Chicago
230 South Dearborn
Chicago, IL 60604-1595

10. SPONSOR/MONITOR'S ACRONYM(S)
ONR

11. SPONSOR/MONITOR'S REPORT NUMBER(S)

12. DISTRIBUTION/AVAILABILITY STATEMENT
Approved for Public Release; distribution is unlimited

13. SUPPLEMENTARY NOTES

14. ABSTRACT
This report summarizes research on two related ONR projects. Award number N00014-11-1-0605 supported the initial portion of our work and was mainly devoted to the effect of 5 at% additions of Cr and/or Pt on the Type II hot corrosion behavior at 700 oC. of β Ni-36Al, an alumina scale-forming alloy. Award number N00014-16-1-2405, a continuation of N00014-11-1-0605, was primarily devoted to the high temperature oxidation of γ/γ' Ni-20Al-5 Cr bond coat alloys; this latter effort had been started on the -0605 program. The -2405 program focused primarily on the effect of small (0.05 at %) additions of the so-called Reactive Elements, Y and Hf to the base γ/γ' Ni-20Al-5Cr bond coat alloy.

15. SUBJECT TERMS

16. SECURITY CLASSIFICATION OF:			17. LIMITATION OF ABSTRACT	18. NUMBER OF PAGES	19a. NAME OF RESPONSIBLE PERSON
a. REPORT	b. ABSTRACT	c. THIS PAGE			
					19b. TELEPHONE NUMBER (Include area code)

Ni-20Al-5Cr-0.05Hf alloys. Double oxidation experiments – oxidation first for 2.5 hrs in [16]O$_2$ followed by 5 hrs in [18]O$_2$ – were next performed on the Ni-20Al-5Cr, Ni-20Al-5Cr-0.05Hf, Ni-20Al-5Cr-0.05Y, and Ni-20Al-5Cr-0.05Hf-0.05Y alloys at temperature between 1100 ^{o}C and 1400 ^{o}C. Following extensive microstructural characterization using SEM and TEM, [18]O depth profiles were determined using high resolution (~100 nm) time of flight – secondary ion mass spectrometry (TOF-SIMS). The extent of new oxide formed at both the scale/gas and scale/metal interfaces allowed understanding of the scaling kinetics in these alloys. Further, the 1400 ^{o}C TOF-SIMS base alloy images clearly showed variability in oxygen grain boundary diffusivities, even for grain boundaries sharing a given grain.

I.2 Grain boundary defects in fully dense Al$_2$O$_3$ and Y$_2$O$_3$-doped Al$_2$O$_3$ polycrystals

Lattice diffusion for both Al and oxygen in α-Al$_2$O$_3$ is so sluggish that all scale growth is dominated by grain boundary diffusion, which is enhanced by a factor of ~10^5 for Al lattice diffusion and a factor of ~10^8 for oxygen lattice diffusion[1]. As discussed in previous publications[1,2], the enhanced grain boundary diffusion is mediated not by point defects, as has been previously assumed, but by a type of grain boundary ledge defect called a disconnection[3], which is characterized by a step height (h) and a Burgers vector ($\vec{b}$), the latter indicating the magnitude of the strain field between the two misfitting grains at a high angle grain boundary. We have utilized a variety of electron microscopy techniques to study disconnections in fully dense polycrystalline Al$_2$O$_3$.

I.3 Hot corrosion of Cr- and Pt-modified NiAl alloys and oxidization of FeCrAl alloys

Hot corrosion of Ni-based and Cr-based alloys occurs between ~ 650 and ~ 900°C in combustion ambients, and is mediated by sulfur in the gas phase and sulfate salts deposited on structural components. This report concerns Type II hot corrosion studies at 700°C of a Cr- or Pt-modified model NiAl alloy, and high temperature double oxidation studies of a FeCrAl alloy, with the [18]O distribution within the scales determined by high spatial resolution (~100 nm) TOF-SIMS. The high temperature oxidation studies were designed to provide fundamental understanding of the kinetic processes governing scale formation.

2

II. Experimental Procedures

II.1 High temperature oxidation of NiAlCr alloys

The NiAlCr alloy samples, whose compositions are shown in Table I, were first cut into 3 mm diameter, 1 mm thick discs. The sample surfaces were prepared using standard metallographic procedures to a 1200-grit finish. High temperature oxidation experiments were conducted at 1100 ^{o}C for 72 hrs. The oxidized samples were cut in the direction perpendicular to the scale growth direction, and the cut surfaces were polished to a surface finish of 1 μm. Scale microstructures were studied in a dual beam focused ion beam/scanning electron microscope (FIB/SEM) (FEI Helios, OR).

Alloy	Composition (at%)
a	Ni-20Al-5Cr
b	Ni-20Al-5Cr-0.05Hf-0.05Y
c	Ni-20Al-5Cr-0.05Hf
d	Ni-20Al-5Cr-0.05Y
e	Ni-20Al-5Cr-1Si
f	Ni-20Al-5Cr-0.05Hf-0.05Y-1Si
g	Ni-20Al-5Cr-0.1Hf-0.05Y
h	Ni-20Al-5Cr-0.1Hf-0.05Y-1Si

Table I Compositions of the eight alloys studied in isothermal oxidation experiments

Double oxidation experiments – oxidation first for 2.5 hrs in $^{16}O_2$ at 200 mbar pressure followed by 5 hrs in $^{18}O_2$, also at 200 mbar pressure– were performed on the Ni-20Al-5Cr and Ni-20Al-5Cr-0.05Hf-0.05Y alloys at 1100, 1200, 1300, and 1400 ^{o}C, and on Ni-20Al-5Cr-0.05Hf and Ni-20Al-5Cr-0.05Y alloys at 1100, 1200, and 1300 ^{o}C. The oxidized

samples were cut and polished at a tilt of 25° in the FIB for TOF-SIMS (PHI TRIFT V Nano TOF, MN) isotopic imaging, as described in our previous work[4]. The oxygen and aluminum grain boundary diffusivities in the Al_2O_3 scales were determined using ^{18}O depth profiles and Le Claire's method[5] for analysis of the of the enhanced grain boundary diffusion "tails." In addition, dual beam SEM-FIB prepared TEM foils from the base alloy, and from the singly doped alloys oxidized at 1100 °C for a total of 7.5 hrs, were used for further microstructural analysis of the oxide scales. Diffraction and EDX analysis were performed in the TEM (FEI Tecnai F30, OR) to study the phase chemistry and elemental distributions in the Al_2O_3 scales.

II.2 Grain boundary line defects

The disconnection grain boundary line defects were studied via transmission Kikuchi diffraction (TKD) in a FIB/SEM (FEI Nova, OR) equipped with an electron back scattering diffraction detector (EBSD) (Oxford Instrument, UK), and in a transmission electron microscope (TEM) (FEI Tecnai F30, OR). TKD samples were taken from the undeformed undoped, deformed undoped, undeformed Y_2O_3-doped, and deformed Y_2O_3-doped Al_2O_3 polycrystals in a FIB/SEM and thinned to a thickness of ~100 nm for TKD data acquisition. TEM samples were prepared using mechanical polishing in a disc polisher and dimpler, followed by final thinning in a precision ion polishing system (PIPS) (Gatan, PA). TEM characterization of the samples were then performed using high resolution TEM imaging.

II.3 Hot corrosion of Cr- and Pt-modified NiAl alloys and oxidization of FeCrAl alloys

The model compositions for the hot corrosion study are of relevance to β-NiAl coatings used as bond coats to protect Ni-based superalloys in service. Model alloys were prepared based on adding 5 at% Cr or Pt to Ni-36 at% Al, with the Type II hot corrosion exposures being conducted by Prof. Brian Gleeson (Univ. of Pittsburgh) at 700°C in flowing O_2 containing 1000 ppm SO_2. Here, we report on the initial stages (2 hr and 20 hr exposures) of Na_2SO_4-induced degradation for the β-Ni-36Al-5Cr, β-Ni-36Al-5Pt, and β- Ni-36Al-5Cr-5Pt alloys. The hot

corrosion exposures were performed with a 2–3 mg/cm^2 deposit of Na$_2$SO$_4$, applied to one of the
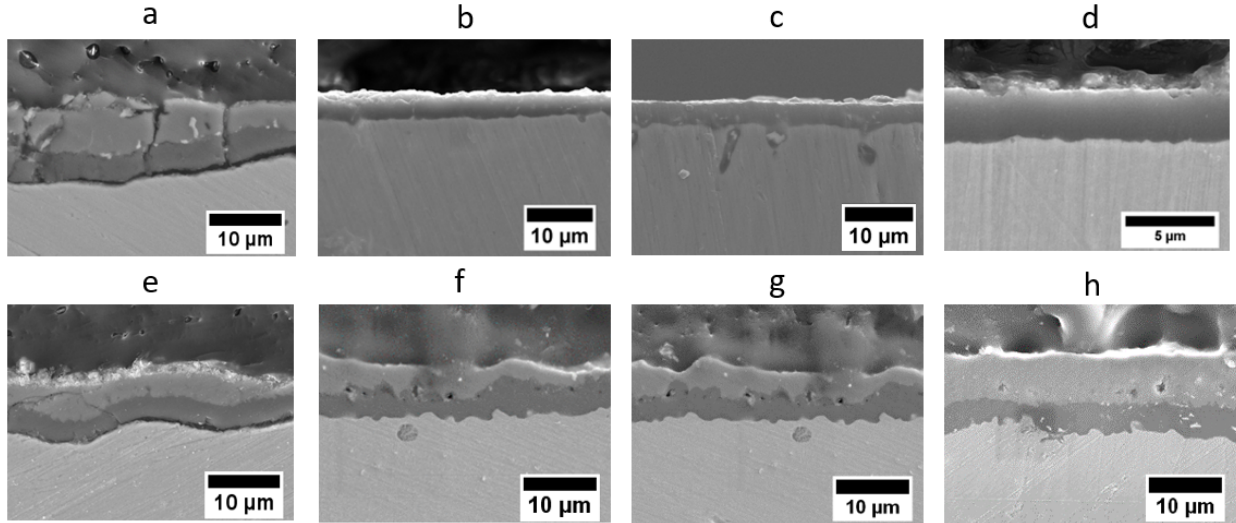

Figure 1 Cross-sectional SEM images of (a) Ni-20Al-5Cr, (b) Ni-20Al-5Cr-0.05Hf-0.05Y, (c)
Ni-20Al-5Cr-0.05Hf, (d) Ni-20Al-5Cr-0.05Y, (e) Ni-20Al-5Cr-1Si, (f)
Ni-20Al-5Cr-0.05Hf-0.05Y-1Si, (g) Ni-20Al-5Cr-0.1Hf-0.05Y, and (h)
Ni-20Al-5Cr-0.1Hf-0.05Y-1Si alloys oxidized at 1100 ^{o}C for 72 hrs in air.

broad surfaces of the specimens.

III. Results

III.1 Isothermal Oxidation Experiments on NiAlCr alloys

As shown in Figs. 1 (a)-(h), the thicknesses of the oxide scales grown on the surface of NiAlCr
alloys ranged between 4 and 12 μm. NiAl$_2$O$_4$ spinel is present as the continuous outer oxide
layer on the base alloy (a), the co-doped alloy containing 1% Si (f), a co-doped alloy containing,
0.05% Y and 0.1% Hf (g), and an alloy of the same composition also containing 1% Si (h).
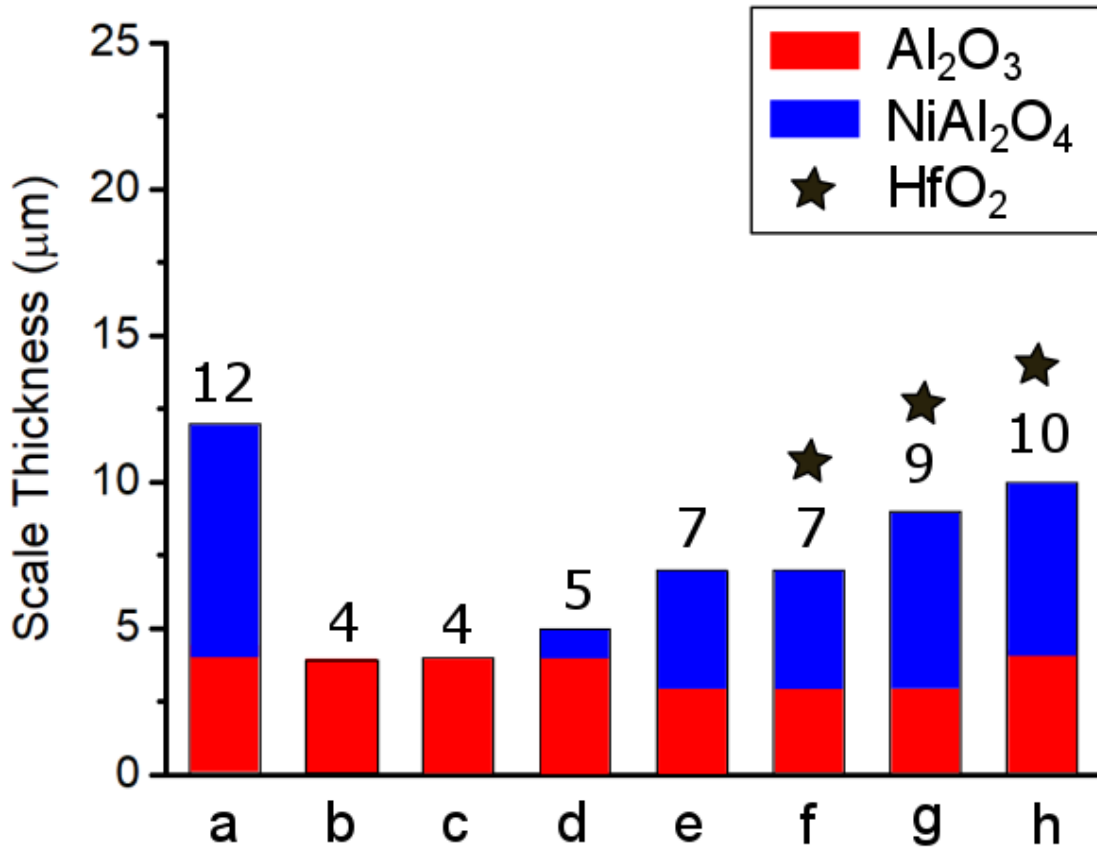
Figure 2 Scale thicknesses measured on the alloys shown in Table I oxidized at 1100 ^{o}C for 72 hrs in laboratory air.

Furthermore, ~1 μm HfO$_2$ precipitates were found in alloys f, g, and h. All the NiAlCr alloys containing small additions of the REs, Hf and Y have better oxidation resistance than the base Ni-20Al-5Cr alloy, as shown in Fig. 2. The thinnest scales, 4 μm, were present on the Ni-20Al-5Cr-0.05Hf and Ni-20Al-5Cr-0.05Hf-0.05Y alloys. This suppression of NiAl$_2$O$_4$ spinel, indicating that suppression of transient oxidation – formation of NiO as the initially formed oxide scale, prior to formation of the stable α-Al$_2$O$_3$ phase – is a very valuable and unexpected consequence of the RE additions.
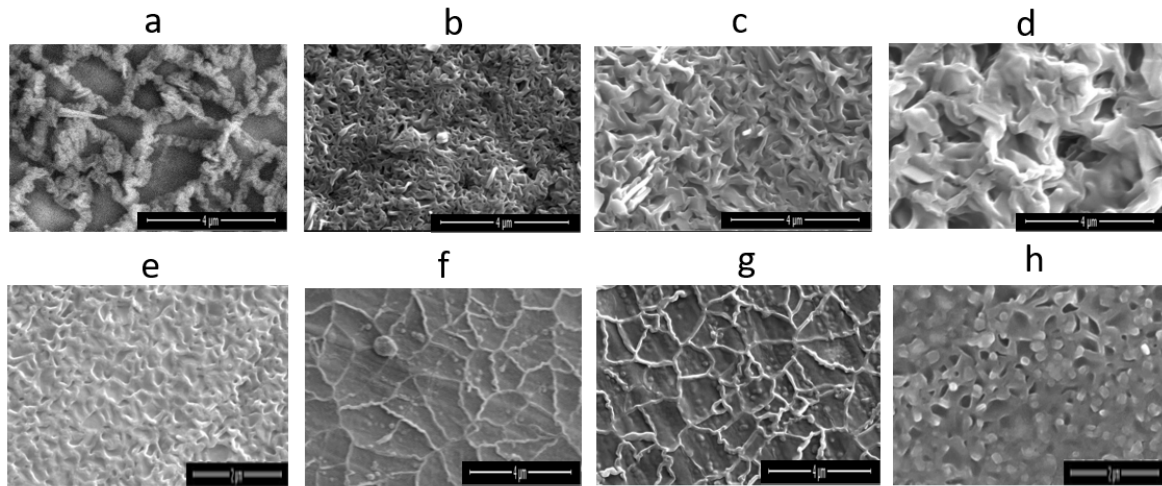
Figure 3 SEM images of the Ni-20Al-5Cr alloy oxidized at (a) 1100 ^{o}C, (b) 1200 ^{o}C, (c) 1300 ^{o}C, and (d) 1400 ^{o}C for a total time of 7.5 hrs, and the Ni-20Al-5Cr-0.05Hf-0.05Y oxidized at (e) 1100 ^{o}C, (f) 1200 ^{o}C, (g) 1300 ^{o}C, and (h) 1400 ^{o}C for a total time of 7.5 hrs

III.2 Double Oxidation Experiments on Ni-20Al-5Cr, Ni-20Al-5Cr-0.05Hf-0.05Y, Ni-20Al-5Cr-0.05Hf, and Ni-20Al-5Cr-0.05Y alloys

Figs. 3 (a)-(d) show the surfaces of the scales on the oxidized Ni-20Al-5Cr and Ni-20Al-5Cr-0.05Hf-0.05Y alloys. Significantly, there is little (<3%) or no spallation. Prominent grain boundary oxide scale ridges are clearly seen in the base alloy oxidized at 1100 ^{o}C (Fig. 3a), and similar surface morphologies were observed on the base alloy oxidized at 1200, 1300, and 1400 ^{o}C. The oxide grain size increases with increasing oxidation temperature, as shown in Figs. 3 (b)-(d). On the other hand, polishing scratches can be observed in Fig. 3 (e), due to a very thin oxide scale. Formation of oxide grain boundary ridges are clearly found in the co-doped (0.05Hf, 0.05Y) samples oxidized at 1200 and 1300 ^{o}C (Figs. 3 (g) and (h)). Porous Al_2O_3 was observed on the top surface of the oxide scale formed at 1400 ^{o}C (Fig. 3 (h)). In general, porous Al_2O_3 scales are usually found at higher temperature, and oxide grain boundary ridges are found in the lower temperature ranges in all four alloy samples. A fully dense Al_2O_3 scale was only found in the co-doped alloy oxidized at 1100 ^{o}C, as shown in Fig, 3 (e).
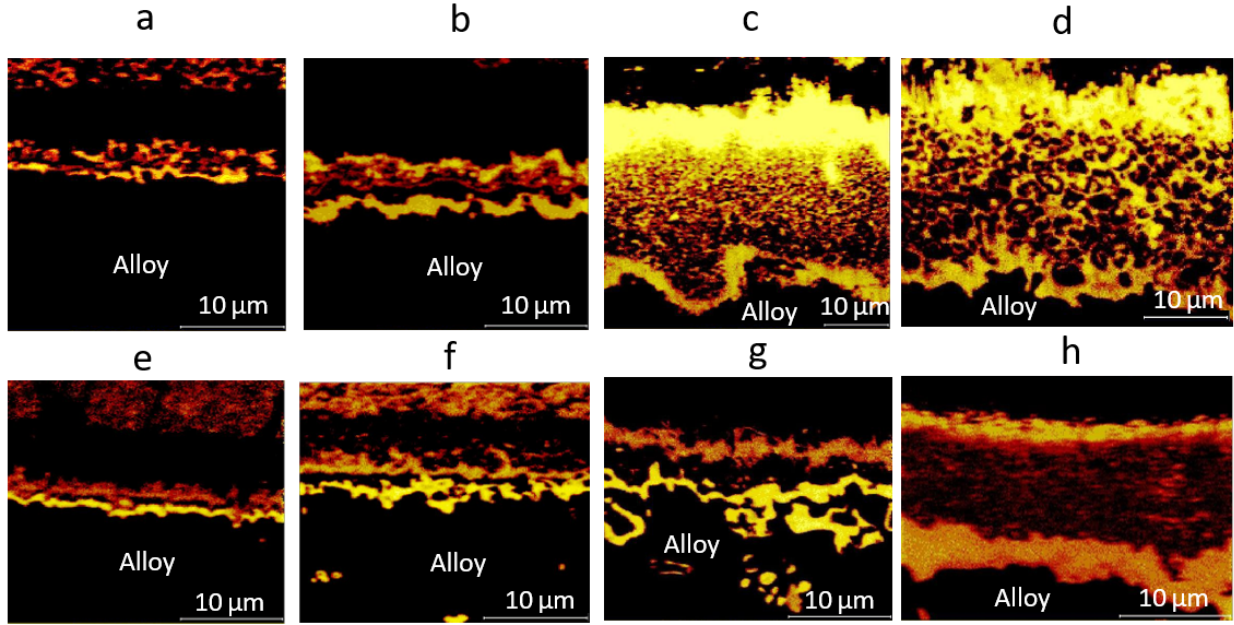
Figure 4 TOF-SIMS images of normalized ^{18}O intensity in the scales formed on Ni-20Al-5Cr alloy at (a) 1100 $^{\circ}$C, (b) 1200 $^{\circ}$C, (c) 1300 $^{\circ}$C, and (d) 1400 $^{\circ}$C, and on the Ni-20Al-5Cr-0.05Hf-0.05Y alloy at (e) 1100 $^{\circ}$C, (f) 1200 $^{\circ}$C, (g) 1300 $^{\circ}$C, and (h) 1400 $^{\circ}$C

III.3 ^{18}O Distribution in Al$_2$O$_3$ scale

TOF-SIMS analyses were performed on FIB-cut surfaces. As shown in Figs. 4 (a)-(h), new oxide formed during the ^{18}O$_2$ oxidation can be observed at both the gas/scale and scale/alloy interfaces in both the base alloy and the co-doped alloy, indicating simultaneous outward diffusion of Al and inward diffusion of oxygen during scale growth. The Al$_2$O$_3$ scale thickness varied between 1 and 11 μm in the base Ni-20Al-5Cr alloy, and between 1 and 6 μm in the co-doped alloy. The thinner oxide scales formed in the co-doped alloy at temperatures above 1100 $^{\circ}$C, compared to the base alloy, is a clear manifestation of the enhanced oxidation resistance afforded by the RE doping.

The ratio of the volume of new oxide at the gas/scale interface to that at the scale/alloy interface, r, decreases with decreasing temperature in the base alloy, while it increases with decreasing temperature in all other RE doped alloys, as shown in Table II. This indicates a larger activation energy for Al grain boundary diffusion than oxygen grain boundary diffusion in the

Ni-20Al-5Cr base alloy. Furthermore, a smaller r value measured in the base alloy compared to

Alloy	Temperature (^{O}C)	Scale thickness (h) (µm) $h_{gas/scale}:h_{scale/alloy}$	r
Ni-20Al-5Cr	1400	2.8:1.8	1.56
Ni-20Al-5Cr	1300	2.3:1.5	1.53
Ni-20Al-5Cr	1200	0.5:0.6	0.83
Ni-20Al-5Cr	1100	0.2:0.3	0.67
Ni-20Al-5Cr-0.05Hf-0.05Y	1400	0.8:1.4	0.57
Ni-20Al-5Cr-0.05Hf-0.05Y	1300	0.7:0.9	0.78
Ni-20Al-5Cr-0.05Hf-0.05Y	1200	0.4:0.3	1.33
Ni-20Al-5Cr-0.05Hf-0.05Y	1100	0.2:0.1	2.00
Ni-20Al-5Cr-0.05Hf	1300	0.9:1.5	0.6
Ni-20Al-5Cr-0.05Hf	1200	0.5:0.6	0.83
Ni-20Al-5Cr-0.05Hf	1100	0.2:0.2	1.00
Ni-20Al-5Cr-0.05Y	1300	1.5:2.2	0.68
Ni-20Al-5Cr-0.05Y	1200	0.9:1.3	0.69
Ni-20Al-5Cr-0.05Y	1100	0.6:0.5	1.20

Table II Scale thicknesses and the ratios, r, of [18]O containing scale at the gas/scale interface and scale/alloy interface in the Ni-20Al-5Cr, Ni-20Al-5Cr-0.05Hf-0.05Y , Ni-20Al-5Cr-0.05Hf and Ni-20Al-5Cr-0.05Y alloys

the Hf-doped, Y-doped, and co-doped alloy at 1300 ^{o}C is clearly a manifestation of reduced outward Al diffusion in the co-doped alloy.

Variable oxygen grain boundaries diffusivity is clearly seen in Fig. 4 (d), even for grain boundaries sharing a given grain. (The smaller grain size in the other samples studied did not allow for such observations but we believe that variable oxygen grain boundary diffusion occurs

in all the oxide scales. Such variable oxygen grain boundary diffusivities had previously been determined in $^{18}O_2$ tracer oxygen experiments in polycrystalline Al_2O_3 ceramics (Nakagawa *et al.* to be published).
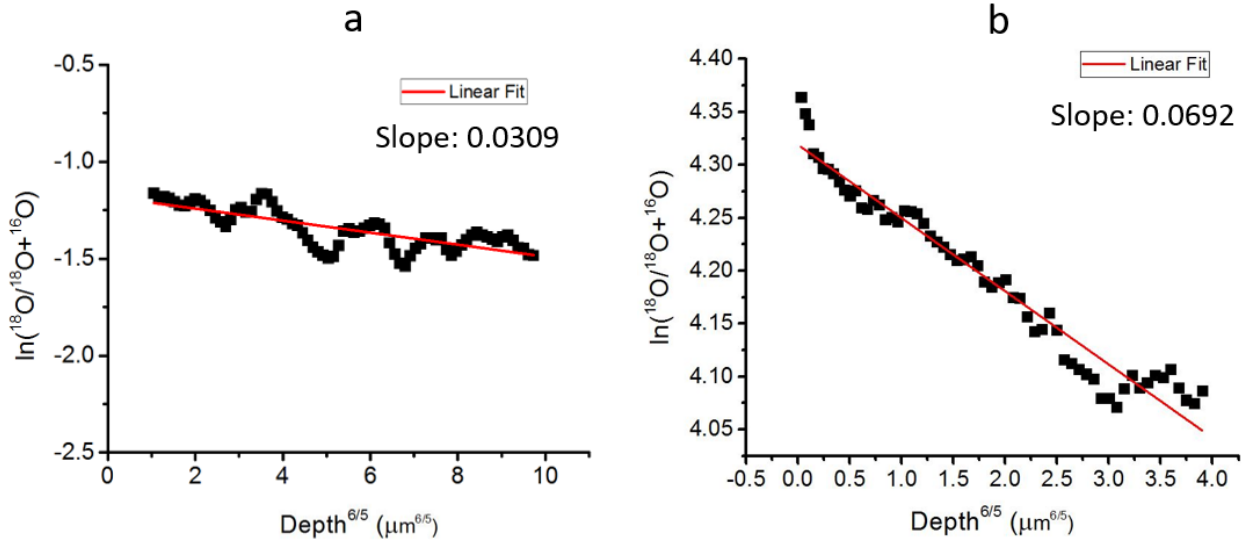
Figure 5 Plots of concentration fraction of $\ln(^{18}O/^{18}O+^{16}O)$ vs depth$^{6/5}$ in (a) the base alloy and (b) the co-doped alloy at 1400 °C for evaluation of $\frac{\partial lnc}{\partial (z)^{6/5}}$ (the slope of the curves) in equation (1)

III.4 Quantitative Determination of Oxygen and Aluminum Grain Boundary Diffusivities

The extent of new oxide formed at the gas/scale and scale/alloy interfaces acquired via TOF-SIMS ^{18}O isotopic imaging allows for determination of oxygen and Al grain boundary diffusivities. The oxygen grain boundary diffusivity (D_{gb}^{Oxy}) is given by the following approximate solution of the diffusion equation developed by Le Claire[5].

$$\delta D_{gb}^{Oxy} = 1.322 \times \left(\frac{D_l^{Oxy}}{t}\right)^{1/2} D_l \times \left(\frac{\partial lnc}{\partial (z)^{6/5}}\right)^{-5/3} \tag{1}$$

where δ is width of grain boundary, assumed to be 1 nm, D_l^{Oxy} is the oxygen lattice diffusivity, t is diffusion time, c is the average ^{18}O concentration, and z is the diffusion distance. D_l^{Oxy} was taken from equation (2):

$$D_l^{Oxy} = 4.6 \times 10^{-3} \, exp\left(-\frac{598 \, [kJ/mol]}{RT}\right) \tag{2}$$

where R is the gas constant, and T is temperature, taken from previous work of Heuer and his collaborators[2,6,7].

The integrated concentration fraction of the $^{18}O/^{18}O+^{16}O$ intensity versus diffusion distance in the base alloy and in the co-doped alloy oxidized at 1400 ^oC are shown in Figs. 5 (a) and (b); the values of $\frac{\partial lnc}{\partial (z)^{6/5}}$ in equation (1) can be determined from the slopes of the curves. (It is noted that the integrated data shown in Fig. 5 (a) and (b) are extracted from the region below the new scale at the gas/scale interface and above the new scale at the scale/alloy interface, which shows the desired ^{18}O gradient.)

The oxygen and Al grain boundary diffusivities at 1400 ^oC are 1×10^{-13} and 5×10^{-13} m^2/s in the Ni-20Al-5Cr alloy, while oxygen and Al grain boundary diffusivities at 1400 ^oC are 1×10^{-14} and 5×10^{-15} m^2/s in the Ni-20Al-5Cr-0.05Hf-0.05Y alloy.

Additionally, Al grain boundary diffusivity can be further determined from Wagner theory[8]:

$$r(T) = \frac{k^{Al}(T)}{k^{Oxy}(T)} \sim \frac{\sqrt{D^{Al}(T)}}{\sqrt{D^{Oxy}(T)}} \tag{3}$$

where r is the ratio shown in Table III, and k^{Al} and k^{Oxy} are parabolic rate constants for Al and oxygen scale growth, respectively.
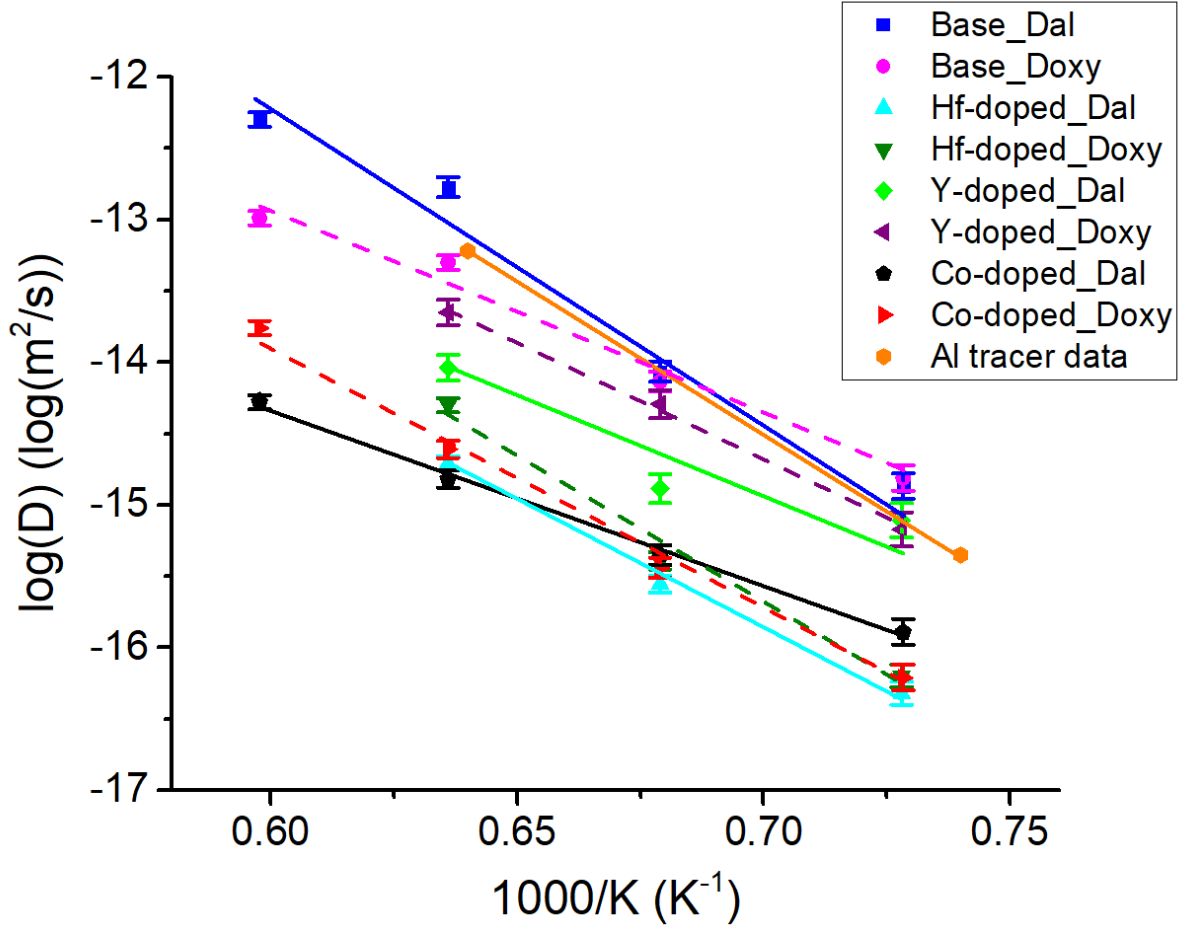
Figure 6 Oxygen and Al grain boundary diffusivities measured in the Ni-20Al-5Cr, Ni-20Al-5Cr-0.05Hf-0.05Y, Ni-20Al-5Cr-0.05Hf, and Ni-20Al-5Cr-0.05Y alloys.

As shown in Fig. 6, the oxygen and Al grain boundary diffusivities in the base alloy are the highest among all the investigated alloys at 1100 – 1400 $^{\circ}$C. Specifically, oxygen and Al grain boundary diffusivities in the base alloy at 1400 $^{\circ}$C are 1.0 x10^{-13} m^2/s and 5.0 x 10^{-13} m^2/s, respectively; the Al grain boundary diffusivity are in remarkably good agreement with recent Al tracer diffusion data[9] in polycrystalline Al$_2$O$_3$. The additions of Hf and Y decrease both oxygen and Al grain boundary diffusivities. The oxygen and Al grain boundary diffusivities in the co-doped alloy at 1400 $^{\circ}$C are 1.3 x10^{-14} m^2/s and 5.0 x 10^{-15} m^2/s. At 1100 $^{\circ}$C, the lowest oxygen and Al grain boundary diffusivities were found in Hf-doped alloy, where D_{gb}^{Oxy} is 6.3 x 10^{-17} m^2/s and D_{gb}^{Al} is 5.0 x 10^{-17} m^2/s, while the oxygen and Al grain boundary diffusivities in the base alloy are at least one order higher than in the Hf-doped alloy. Both

oxygen and Al grain boundary diffusivities at 1300 ^{o}C indicate base alloy > Y-doped alloy >

Hf-doped alloy > co-doped alloy, while they follow base alloy > Y-doped alloy > co-doped alloy

> Hf-doped alloy at 1100 ^{o}C.

Alloys \ Activation energy (Q) (kJ/mol)	Q_{gb}^{Al}	Q_{gb}^{Oxy}
Ni-20Al-5Cr	400±37	280±26
Ni-20Al-5Cr-0.05Hf	340±22	390±25
Ni-20Al-5Cr-0.05Y	230±12	310±16
Ni-20Al-5Cr-0.05Hf-0.05Y	220±13	370±21

Table III Activation energy of Al and oxygen grain boundary diffusion in Al_2O_3 scale in the Ni-20Al-5Cr, Ni-20Al-5Cr-0.05Hf, Ni-20Al-5Cr-0.05Y, and Ni-20Al-5Cr-0.05Hf-0.05Y alloys

Furthermore, as shown in Table III, the Al grain boundary diffusion activation energy (Q^{Al} = 400 ±37 kJ/mol) is significantly higher than the oxygen diffusion activation energy (Q^{Oxy} = 280 ±26 kJ/mol) in the base alloy. Surprisingly, the Al grain boundary diffusion activation energies measured in the Hf-doped, Y-doped, and co-doped alloys are lower than the oxygen diffusion activation energies, a further manifestation of the RE effect.

There are only limited data for oxygen and Al grain boundary diffusion in the literature. In this work, the oxygen grain boundary diffusivities in the reactive element-doped alloys are significantly lower than Al tracer data. Taking all the grain boundary diffusivities into account, and as discussed in our previous work[1], this is believed due to the REs modifying the density of states of the Al_2O_3 scale. It then follows that the kinetics of oxidation are controlled not solely by oxygen and/or Al mass transport, as has previously been assumed; the electronic conductivity of the Al_2O_3 scale cannot be ignored when considering scale growth.

III.5 TEM characterization of the Al$_2$O$_3$ scales

TEM characterization of the Al$_2$O$_3$ scales were performed on the Y-doped and Hf-doped alloys. As shown in Fig. 7 (a), columnar α-Al$_2$O$_3$ grains with a grain size of 100-200 nm are found near the scale/alloy interface in the Y-doped alloy. 100-300 nm grains of NiAl$_2$O$_4$ spinel formed during the initial stage of oxidation near the scale/gas interface in the Y-doped and the Hf-doped alloys. As indicated in Fig. 7 (b), the image and corresponding energy dispersive x-ray spectroscopy (EDX) spectrum, 5-30 nm Y$_2$O$_3$ nano-precipitates are present at ~ 200-300 nm away from the scale/alloy interface. Similar scale morphologies -- columnar α-Al$_2$O$_3$ grains near the scale/alloy interface and scattered spinel crystallites near the gas/scale interface -- is observed in the Hf-doped alloy. In Fig. 8, a high angle angular dark field (HAADF) image acquired in the scanning transmission electron microscopy (STEM) mode shows that a band of 5-20 nm HfO$_2$ precipitates is found 100-200 nm away from the scale/alloy interface in the Hf-doped alloy. Furthers, Hf enrichment at the grain boundaries between columnar grains and scale/alloy interface are observed in the corresponding Hf EDX maps, indicating Hf segregation to grain boundaries in the Al$_2$O$_3$ scale grown on the Hf-doped alloy, as ezpected.

(a)

NiAl$_2$O$_4$ ZA: [210]

α-Al$_2$O$_3$ ZA: [10$\bar{1}$0]

Alloy

Scale

Pt

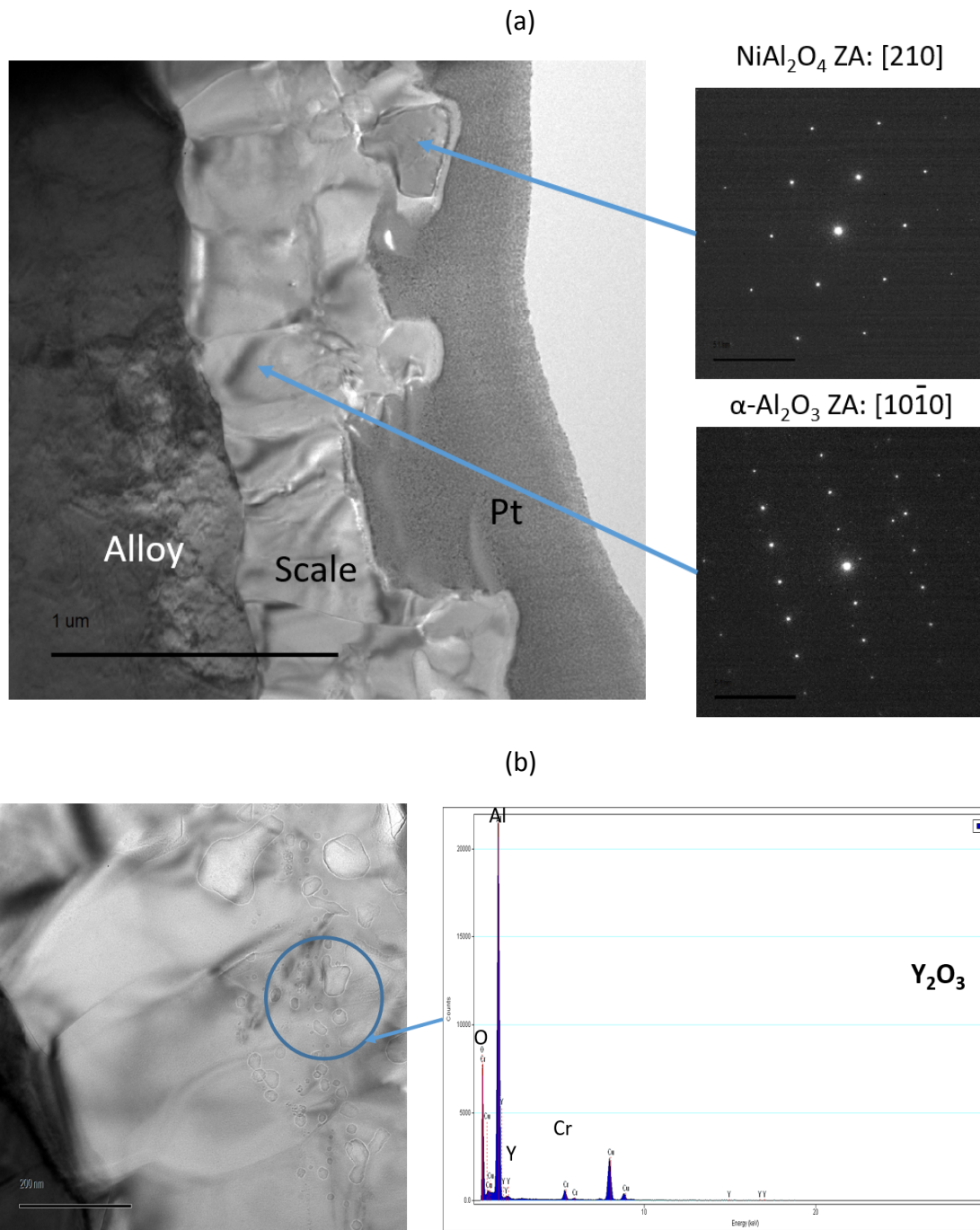1 um

(b)

Y$_2$O$_3$

Al

O

Cr

Y

200 nm

Figure 7 (a) TEM bright-field image and diffraction patterns from the selected grains in the Al$_2$O$_3$ scale on the Ni-20Al-5Cr-0.05Y alloy oxidized at 1100 $^\circ$C for a total of 7.5 hrs. (b) TEM bright-field image of the scale near scale/alloy interface. The EDX spectrum on the right acquired from the circled area indicates the existence of small Y$_2$O$_3$ precipitates within the scale.
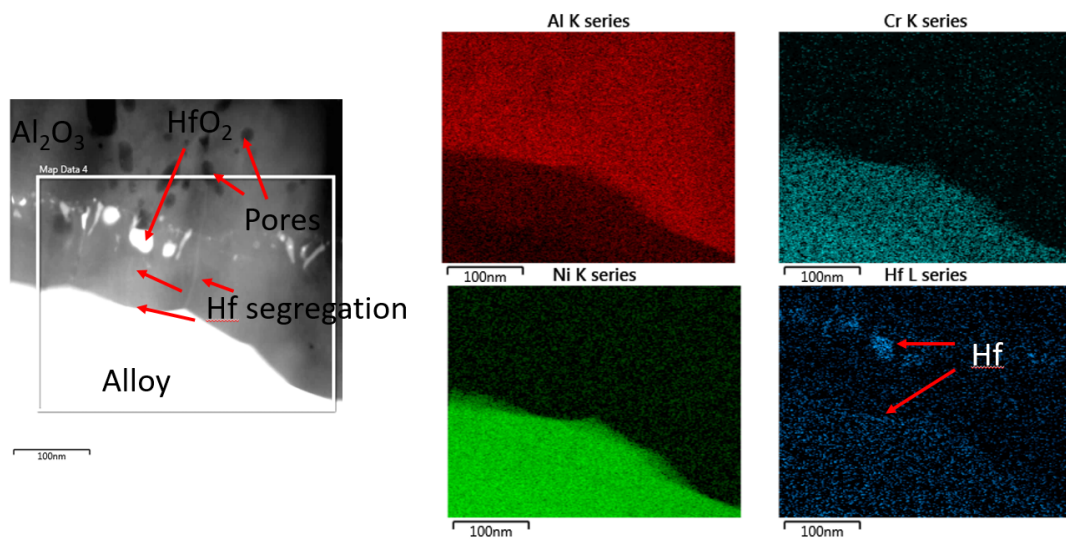
Figure 8 HAADF STEM image of Al$_2$O$_3$ scale on Ni-20Al-5Cr-0.05Hf alloy oxidized at 1100 ^{o}C for a total of 7.5 hrs. The corresponding Al, Cr, Ni, and Hf EDX maps of the boxed area are shown on the right.
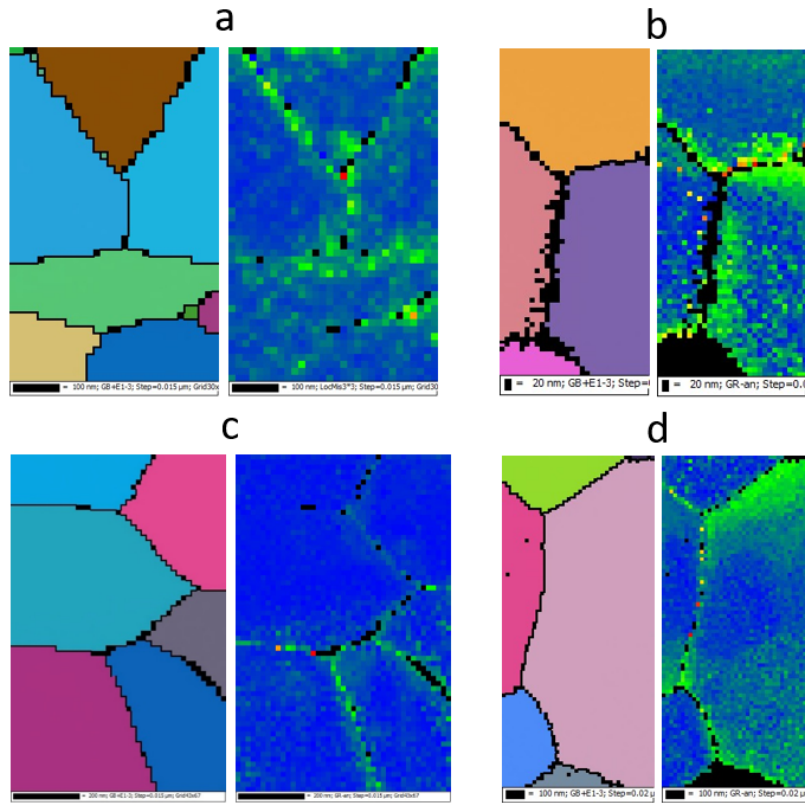
Figure 9 TKD orientation maps (left) and the corresponding crystallographic misorientation maps (right) in (a) undeformed undoped Al_2O_3, (b) deformed undoped Al_2O_3, (c) undeformed Y-doped Al_2O_3, and (d) deformed Y-doped Al_2O_3

III.6 TKD and TEM Characterization of Disconnections

Both undoped Al_2O_3 and Al_2O_3 doped with 0.1% Y_2O_3 have been studied in the as-sintered state and after 2% plastic deformation. Both the sintering and the plastic deformation were conducted at 1300 ^{o}C.

TKD analysis of the four dense polycrystalline Al_2O_3 samples is shown in Figs. 9 (a)-(d). Misorientation in crystallographic orientation (~0.3-0.5 degrees, the green areas) within a given area near the grain boundaries is observed in all samples, although there is variability in the areas showing such misorientation. The near-grain boundary crystallographic misorientations indicate the presence of grain boundary line defects - disconnections, dislocations, and disclinations.

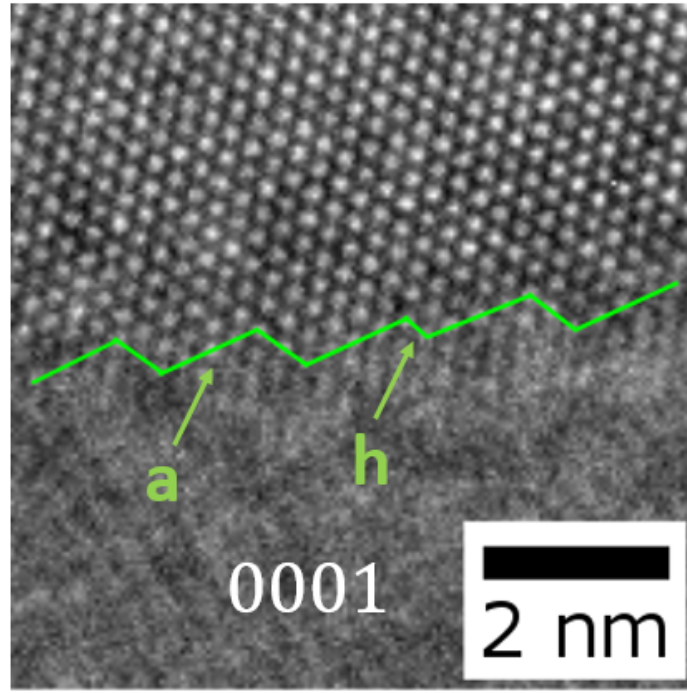Characterization of the disconnections was further performed for all samples in the TEM,

Figure 10 High resolution TEM image of disconnections in undeformed undoped Al_2O_3. The viewing direction for the upper grain is parallel to [0001].

Average Number	Undeformed Al_2O_3	Deformed Al_2O_3	Undeformed Y-doped Al_2O_3	Deformed Y-doped Al_2O_3
Step Ratio	0.52	0.46	0.44	0.36
Step Height (μm)	0.91	0.89	0.48	0.55
Step Interval (μm)	1.70	1.86	1.01	1.51

Table IV Statistical data of step ratio, step height, and step interval of disconnections in undeformed Al_2O_3, deformed Al_2O_3, undeformed Y-doped Al_2O_3, deformed Y-doped Al_2O_3. The data were collected from at least 100 measurements in each sample.

determining step height (h) and step interval (a) (see Fig. 10) in over 100 grain boundary disconnections in each of the four samples. As shown in Table IV, the average step ratios, h/a, are lower in the deformed samples in both the undoped and Y-doped samples, while the average step intervals are longer in the deformed samples. Such quantitative data is needed for developing high temperature creep models.
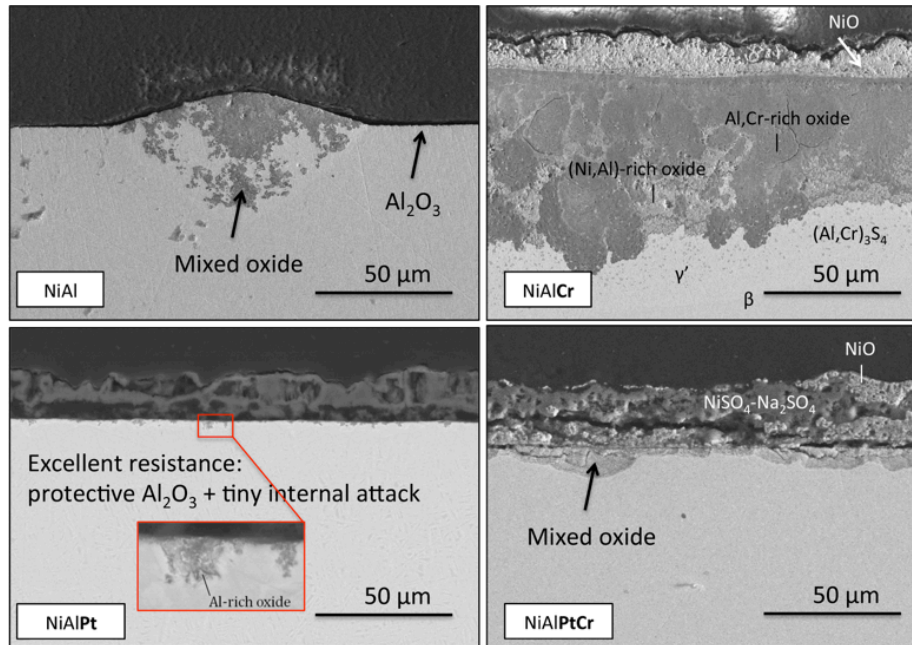
Figure 11 Corrosion products developed after 20 h exposure to Na_2SO_4 in O_2-SO_2 at 700°C.

III.7 Hot corrosion of Cr- and Pt-modified NiAl alloys

The cross section of the four alloys in Fig. 11 after exposure for 20 hrs at 700 °C in the O_2 +1000 ppm SO_2 gas ambient shows the extent of the early stages of Na_2SO_4-induced degradation, and can serve as a summary of our work. With addition of 5 at % Cr or 5 at % Pt to the base alloy, the oxide layer with locally growing nodules has completely transformed to uniform but rapid growing attack (the Cr addition) or to a very slow growing thin oxide (Pt addition), while the quaternary alloy has characteristics of both ternary alloys. The structure of corrosion products of each alloy after 2 or 20 hours of Na_2SO_4-induced exposure will now be discussed.
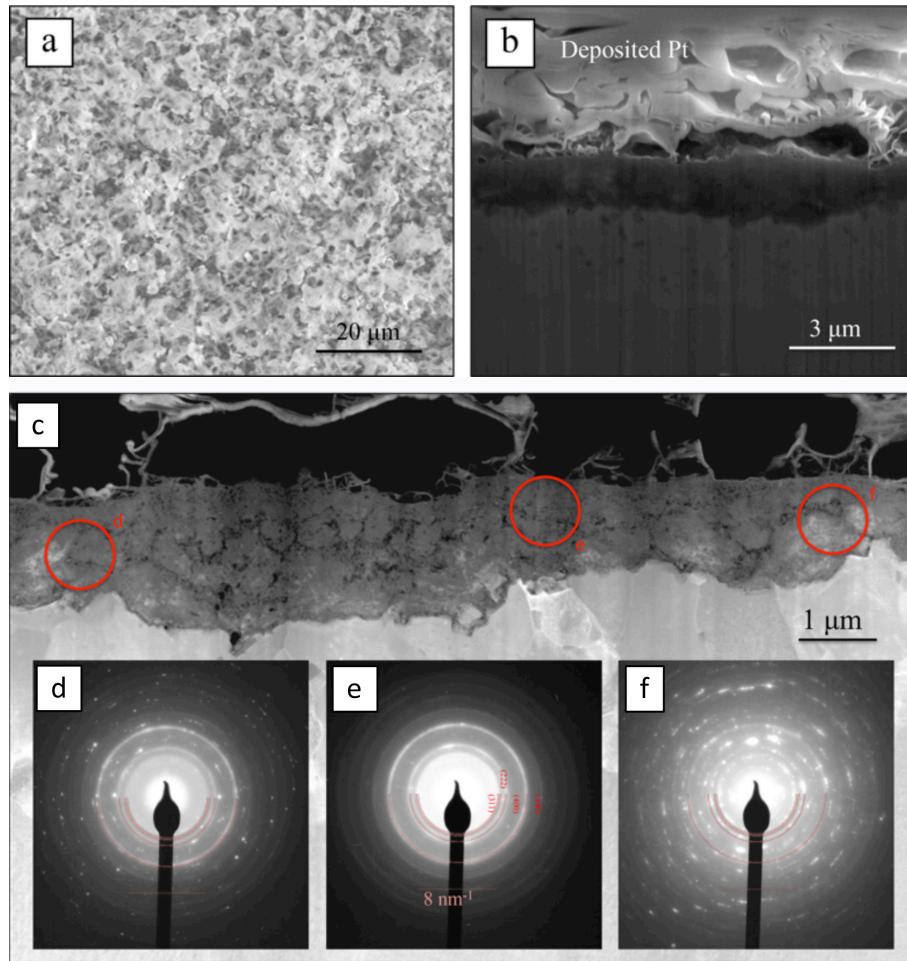
Figure 12 SEM images of NiAlCr alloy after 2 hrs exposure to Na_2SO_4 in O_2-SO_2 at 700°C, a) surface view, b) cross section view; c) STEM image and e-f) SAD pattern from different areas of the scale. The red circles show the location of SAD aperture. Simulated γ-Al_2O_3 ring patterns are overlaid on DPs.

III.7.1 Ni-36Al-5Cr

The microstructure of the corrosion products formed in Ni-36Al-5Cr sample after 2 hrs is shown in Fig. 12. The surface was covered with a uniform but very porous oxide; the degradation was extensive. A TEM FIB lift-out sample (Figs. 12 (c) - (f)) reveals that the scale mostly has the γ-Al_2O_3 structure, but a mixture of different sulfides and oxides was present close to the oxide/metal interface.

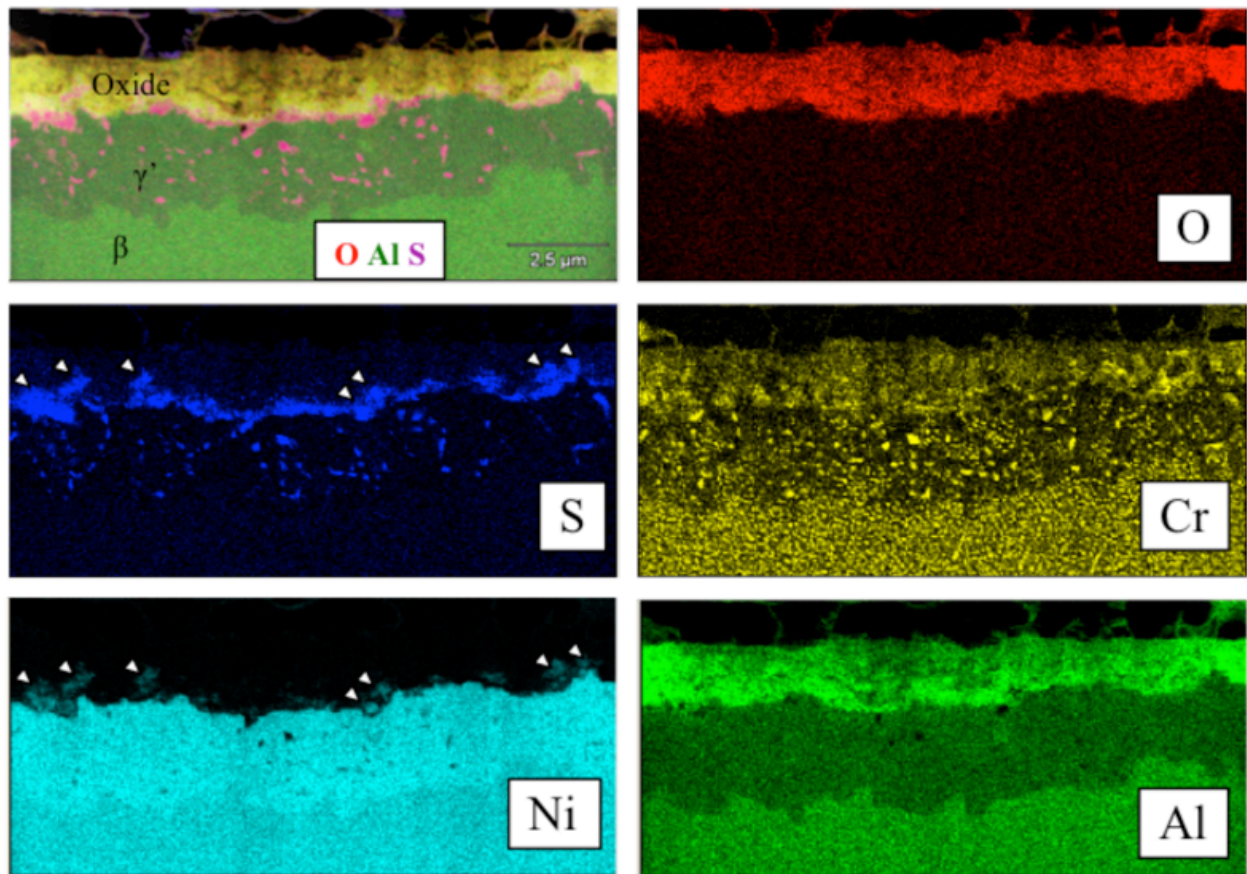Figure 13 Distribution of main elements in the reaction front of NiAlCr alloy after 2 hrs exposure to Na_2SO_4 in O_2-SO_2 at 700°C, Green: Al, Pink: S, Red: O, Yellow: Al_2O_3 (Red + Green = Yellow).

TEM-EDS elemental maps are presented in Fig. 13. The oxide contains both Al and Cr but not Ni, and the "γ-Al_2O_3" present is clearly an Al/Cr solid solution. A significant sulfur concentration (~24 at% S) was present near the oxide/metal interface, as well as Ni_3S_2 particles. Cr-rich sulfides and α-Cr precipitates were present in the Al-depleted γ' matrix below the oxide.
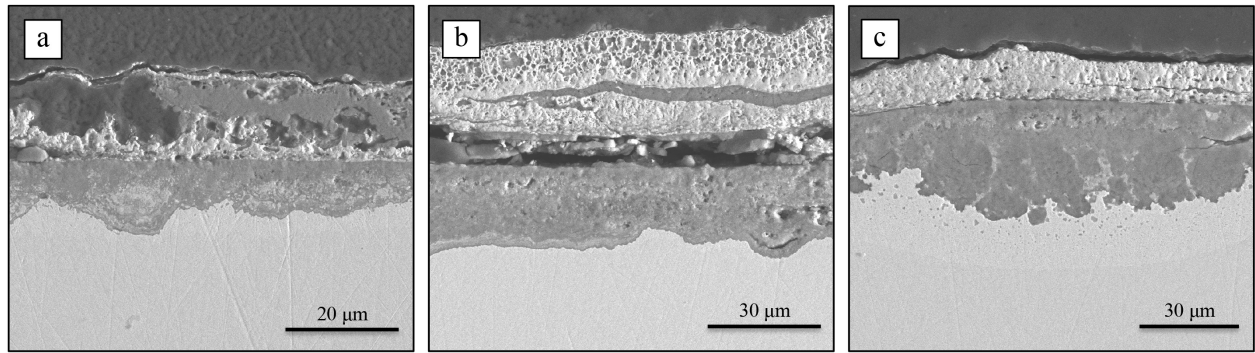
Figure 14: Ni-36Al-5Cr after 20 h exposure to Na_2SO_4 in O_2-SO_2 at 700°C, SEM (BSE) images. (a) to (c) represent the different corrosion product thicknesses observed on the same sample.

The corrosion products of the 20 hr NiAlCr sample were similar; sustained degradation was observed, characterized by sulfide precipitation in an Al-depleted γ' matrix at the reaction front and growth of an Al-rich, S-containing porous oxide layer. Some NiO was present at the oxide/salt interface, and in some regions, its dissolution in the salt and its re-precipitation at the salt/gas interface could be observed. This morphology has some similarity to Type I hot corrosion where the Na_2SO_4-salt is liquid. Zones of varying thicknesses but equivalent morphologies were observed (Figs. 14 (a)-(c)).
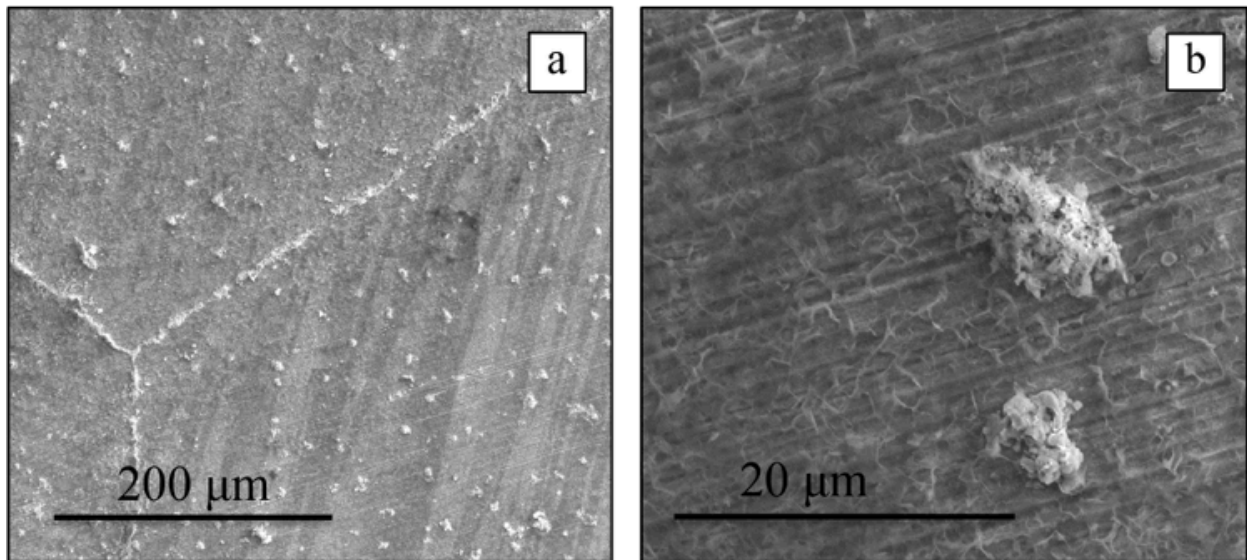
Figure 15: NiAlPt after 2 h hot corrosion. (a) SEM surface view, (b) SEM higher mag, (c) the location of prepared TEM sample, (d) STEM cross-section view of the prepared sample.

III.7.2 Ni-36Al-5Pt

The Ni-36Al-5Pt sample after 2 h exposure to Na_2SO_4 and O_2 +1000 ppm SO_2 at 700°C formed a uniform and dense Al_2O_3 scale, but some enhanced surface attack occurred randomly on the surface (Figs. 15 (a) and (b)); however, these small porous protrusions had not penetrated very deeply into the alloy. There did appear to be preferential formation of these protrusions on the grain boundaries.

Degradation of the NiAlPt alloy after 20 hr exposure to Na_2SO_4 and O_2 +1000 ppm SO_2 at 700°C also occurred non-uniformly (Fig. 16), the alloy forming a dense external Al_2O_3 scale, albeit with small pits of Al-rich oxide extending into the alloy. TEM characterization (Figs. 16 (d) and (e)) showed that the oxide was a dense, single phase Ni-free γ-Al_2O_3. Further, individual equi-axed Pt particles were incorporated in the relatively pure γ-Al_2O_3 scale (Fig. 16 (d)).
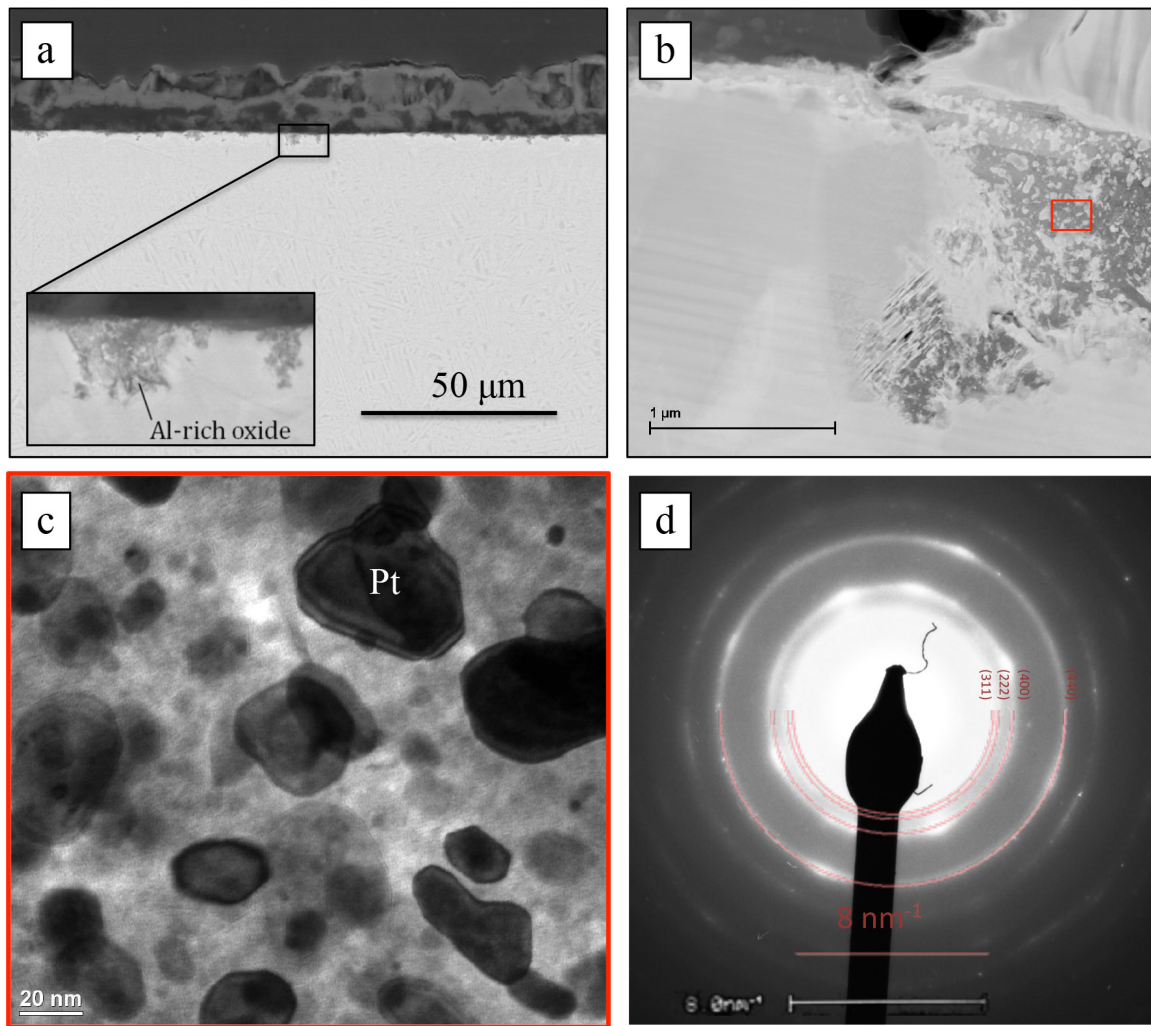
Figure 16: NiAlPt after 20 h hot corrosion, a) SEM (BSE) image showing small protrusions growing into the alloy, b) STEM image of the oxide protrusion; c) bright field TEM image of the oxide formed in the protrusion, d) diffraction pattern of sub-micron crystals of oxide in NiAlPt alloy after 20 h hot corrosion, indexed to γ-Al_2O_3.

However, the overall resistance to Na_2SO_4–induced degradation was excellent. Similar to the NiAl alloy, inward growth of oxide was observed in this sample, but the oxidation rate was much lower. Despite the fact that protrusions formed more frequently on the surface in this alloy, the large nodules, which were observed on NiAl alloy, were not observed.

III.7.3 Discussion: Cr and Pt effects on hot corrosion resistance

Pt dramatically increased the hot corrosion resistance of the NiAl alloy. Pt aids in oxide scale adherence and promotes exclusive Al_2O_3 scales. Ultimately, the removal of Pt from the composition is desirable from a cost perspective, but in this work, it has been demonstrated that the protection required for high temperature operation has been achieved with a comparatively low level of Pt.

Early-stage hot corrosion changed from local to uniform attack with 5 at% addition of Cr to the Ni-36Al alloy. In the Cr-containing alloy, porous non-protective scales formed; moreover, dissolution of corrosion products in the salt decreased the melting temperature and the eutectic liquid formed uniformly on the surface, which accelerated the rate of hot corrosion. Further, the dissolution and re-deposition of NiO in the salt was observed in the corrosion products of this alloy, which shows that the salt chemistry can affect the mechanism of initiation and growth of the oxide layer.

Thus, Pt and Cr affect the early stages of Type II hot corrosion in two different ways; Pt improves the corrosion resistance by forming a dense slow-growing oxide layer, while Cr changes the attack from local to uniform.

IV. References

1.   Heuer, A. H. *et al.* The Band Structure of Polycrystalline Al_2O_3 and its Influence on Transport Phenomena. *J. Am. Ceram. Soc.* **15,** 1–15 (2016).

2.   Heuer, A. H. and Zahiri Azar, M. A disconnection mechanism of enhanced grain boundary diffusion in Al2O3. *Scr. Mater.* **102,** 15–18 (2015).

3.   Hirth, J. P. Dislocations, steps and disconnections at interfaces. *J. Phys. Chem. Solids* **55,** 985–989 (1994).

4.   Abbasi, K., Zahiri Azar, M.   and Heuer, A. H. Study of scale formation on Al_2O_3-scale forming alloys by time-of-flight secondary ion mass spectrometry (TOF-SIMS). *Mater. Perform. Charact.* **6,** 292–297 (2017).

5.   LeClaire, A. D. The analysis of grain boundary diffusion measurements. *Br. J. Appl. Phys.* **14,** 351–356 (1963).

6.   Heuer, A. H. Oxygen and aluminum diffusion in α-Al$_2$O$_3$: How much do we really understand? *J. Eur. Ceram. Soc.* **28,** 1495–1507 (2008).

7.   Heuer, A. H., Hovis, D. B., Smialek, J. L. &Gleeson, B. Alumina Scale Formation: A New Perspective. *J. Am. Ceram. Soc.* **94,** 146–153 (2011).

8.   Wagner, C. Contributions to the Theory of the Tarnishing Process. *Z. Phys. Chem.* **B21,** 25–41 (1933).

9.   Fielitz, P., Kelm, K., Bertram, R., Chokshi, A. H. &Borchardt, G. Acta Materialia Aluminium-26 grain boundary diffusion in pure and Y-doped polycrystalline a -alumina. *Acta Mater.* **127,** 302–311 (2017).